Journal of Polymer Science

WILEY

JOURNAL OF POLYMER SCIENCE

RESEARCH ARTICLE OPEN ACCESS

Combining Crystallization- and Stereocomplex-Driven Self-Assembly for the Selective Loading of Patchy Worm-Like Core-Crystalline Micelles

Roman Schaller[1] | Emma Fuchs[1] | Lisa Maria Günther[2,3] | Holger Schmalz[1,3]

[1]Macromolecular Chemistry, University of Bayreuth, Bayreuth, Germany | [2]Spectroscopy of Soft Matter, University of Bayreuth, Bayreuth, Germany | [3]Bavarian Polymer Institute, University of Bayreuth, Bayreuth, Germany

Correspondence: Holger Schmalz (holger.schmalz@uni-bayreuth.de)

Received: 29 January 2025 | **Revised:** 17 March 2025 | **Accepted:** 25 March 2025

Funding: This work was supported by Deutsche Forschungsgemeinschaft, SCHM2428/3-1.

Keywords: anionic polymerization | block copolymers | crystallization-driven self-assembly | fluorescence correlation spectroscopy | fluorescence labeling | patchy micelles | stereocomplex-driven self-assembly

ABSTRACT

Micelles with a patch-like microphase-separated (patchy) corona are of increasing interest as their unique corona structure opens various applications, for example, as emulsion stabilizers, blend compatibilizers, nanoparticle templates for catalysis, or hierarchical self-assembly. Crystallization-driven self-assembly (CDSA) is an efficient method for the preparation of patchy core-crystalline micelles (CCMs). However, so far studies mainly focus on CCMs with amorphous corona blocks. In this work, a combination of CDSA with stereocomplex-driven self-assembly (SCDSA) is employed to selectively load stereoregular poly(*L*-lactide) patches in the corona of worm-like CCMs (wCCMs) formed by a double-crystalline polystyrene-*block*-polyethylene-*block*-poly(*L*-lactide) (PS-*b*-PE-*b*-P*L*LA) triblock terpolymer. Well-defined wCCMs with an amorphous patchy PS/P*L*LA corona are formed by CDSA in a good solvent for the PS and P*L*LA blocks, that is, P*L*LA crystallization is hindered within the patches. However, decreasing the solvent quality for the P*L*LA block can induce crystallization within the partially collapsed P*L*LA patches, although the degree of crystallinity is comparably low (< 5%). SCDSA of the patchy wCCMs with an enantiomeric poly(*D*-lactide) homopolymer is utilized to selectively form polylactide stereocomplexes within the patchy corona and, furthermore, to introduce a fluorescence dye, allowing the use of fluorescence correlation spectroscopy to study stereocomplex formation directly in dispersion.

1 | Introduction

Surface-compartmentalized polymer micelles have attracted considerable interest due to their unique corona structure, which can be harnessed for a wide range of relevant applications [1–11]. Generally, they can be divided into Janus micelles featuring two opposing faces with different chemistry and/or polarity [12–18], and patchy micelles that are characterized by a patch-like microphase-separated corona consisting of several compartments with distinct properties [1, 7, 8, 19, 20]. Janus micelles have been utilized in numerous applications, for example, as biosensors and optical nanoprobes [21, 22], as efficient stabilizers for emulsions [23–25], for the compatibilization of polymer blends [26–29], in interfacial catalysis [30, 31], and many more. For patchy micelles, however, the main research focus so far was laid on their preparation and hierarchical self-assembly [32–38], and reports on the application of patchy micelles/particles are scarce. The patchy corona can serve as a template for the regioselective incorporation of nanoparticles, enabling applications in heterogeneous catalysis [39–42], or for constructing hierarchical superstructures when combined with supramolecular self-assembly [43, 44].

Crystallization-driven self-assembly (CDSA) has proven a powerful tool to produce well-defined one-dimensional (cylindrical/worm-like) surface-compartmentalized micelles and can also be performed in a living manner, which allows control over length, length distribution, and corona chemistry [45–49]. While, up to now, mostly triblock terpolymers with a crystallizable middle block based on polyethylene or polyferrocenyldimethylsilane linked to two amorphous and incompatible corona-forming blocks were used [50–52], there are considerably fewer studies on CDSA of triblock copolymers featuring two crystallizable blocks [53, 54]. In recent years, CDSA of conjugated polymers became more and more popular; however, reports on double-crystalline diblock co- and triblock terpolymers remain scarce [55–58]. If next to the core-forming block, also one of the corona-forming blocks is able to crystallize, two important questions arise: Does crystallization of the corona block influence CDSA, resulting in different micellar morphologies? And is crystallization within a microphase-separated corona (Janus-type or patchy) still possible, or impeded by the exerted confinement? Recent work on the self-assembly of double-crystalline poly(ε-caprolactone)-*block*-poly(*p*-dioxanone)-*block*-poly(*N*,*N*-dimethyl acrylamide) (PCL-*b*-PPDO-*b*-PDMA) triblock terpolymers might give possible answers to these questions. In this study, seeded growth experiments with PPDO-*b*-PDMA seeds led only to the crystallization of the PPDO block, while PCL stayed amorphous due to the confinement exerted when PPDO crystals were formed first (overcrowding of PCL chains tethered on the PPDO platelet surface) [59].

Besides, stereocomplex-driven self-assembly (SCDSA) between enantiomeric block copolymers based on poly(*L*-lactide) (P*L*LA) and poly(*D*-lactide) (P*D*LA) has emerged as another efficient route for the preparation of core-crystalline micelles with insoluble P*L*LA/P*D*LA stereocomplex (SC) cores [60, 61]. Most studies are based on water-soluble SC micelles employing linear block copolymers (AB-, ABA-, and ABC-type), star-shaped block copolymers, and graft copolymers with poly(ethylene oxide) (PEO) or poly(oligo(ethylene glycol) methacrylate) [62–67]. Alternatively, block copolymers with poly(acrylic acid) [68, 69], poly(*N*,*N*-dimethylaminoethyl methacrylate) [70, 71], poly(*N*-*iso*propyl acrylamide) [72], or poly(*iso*glycerol methacrylate) [73] blocks were used. Interestingly, mixing of cylindrical micelle dispersions with enantiomeric P*L*LA or P*D*LA cores induced a stereocomplex-driven morphological transition to spherical micelles, whereby the solubility of the employed diblock or triblock copolymers played an important role [69, 74]. On the contrary, there are only a limited number of reports on SCDSA in organic solvents [75–77]. Nonetheless, SCDSA in organic solvents can be a highly versatile strategy, as recently shown by the preparation of patchy SC micelles showing superior interfacial activity and performance as blend compatibilizers [78, 79].

Herein, we report the preparation of patchy worm-like core-crystalline micelles (wCCMs) with SC compartments by combining CDSA and SCDSA of a double-crystalline polystyrene-*block*-polyethylene-*block*-poly(*L*-lactide) (SEL) triblock terpolymer (Scheme 1). Next to the synthesis and characterization of the triblock terpolymers, the influence of solvent on CDSA to patchy wCCMs as well as on crystallization

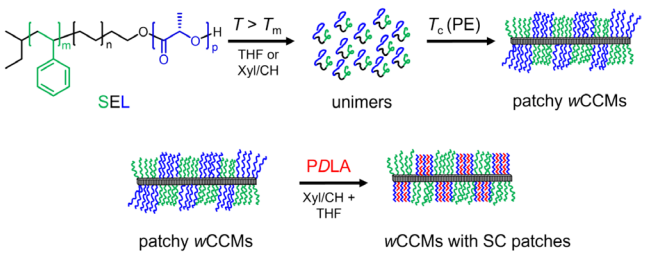

SCHEME 1 | Schematic illustration of the preparation of patchy wCCMs by CDSA of SEL triblock terpolymers (top). SCDSA with P*D*LA homopolymer results in the formation of P*L*LA/P*D*LA SC patches within the corona (bottom).

within the P*L*LA patches is addressed. Moreover, SCDSA of the patchy SEL wCCMs with an enantiomeric P*D*LA homopolymer is employed to selectively load the P*L*LA patches of the micelles. This is utilized to functionalize the SC patches in the wCCM corona with a fluorescence dye, enabling the verification of SC formation directly in dispersion by fluorescence correlation spectroscopy.

2 | Results and Discussion

2.1 | Synthesis of SEL Triblock Terpolymers

The SEL triblock terpolymers were synthesized by a combination of living anionic polymerization, organo-catalyzed ring-opening polymerization (ROP), and catalytic hydrogenation, as shown in Scheme 2. First, a hydroxy end-functionalized polystyrene-*block*-poly(1,4-butadiene) (SB-OH) diblock copolymer was prepared by sequential living anionic polymerization of styrene and 1,3-butadiene in toluene, using *sec*-butyllithium as the initiator, followed by end-capping with ethylene oxide (Scheme 2A) [80]. The combination of an organolithium initiator with toluene as a nonpolar solvent yields a polybutadiene (PB) block with a high fraction of 1,4-PB units (ca. 90 mol-%, Table 1), which is essential to get a pseudo polyethylene (PE) block after hydrogenation. The SB-OH diblock copolymer was then used as a macroinitiator for the organo-catalyzed ROP of *L*-lactide, employing 1,8-diazabicyclo[5.4.0]undec-7-ene (DBU) as a catalyst, which yielded the respective polystyrene-*block*-poly(1,4-butadiene)-*block*-poly(*L*-lactide) (SBL) triblock terpolymers. A detailed description of the syntheses and the employed materials is provided in the Section 4.

The molecular characteristics of the synthesized SBL triblock terpolymers and the respective SB-OH precursor are summarized in Table 1. In the used nomenclature, for example, $S_{296}B_{312}L_{368}$ (SBL-1), the indices correspond to the number-average degrees of polymerization of the respective blocks. Figure 1 shows as an example the apparent molecular weight distributions of SBL-2 together with the corresponding PS and SB-OH precursors as determined by size exclusion chromatography (SEC, results for SBL-1 are given in Figure S1B). The SEC results indicate that the synthesis has proceeded without significant side reactions, yielding a narrowly distributed SBL triblock terpolymer with a dispersity of $Đ = 1.10$. Only upon addition of 1,3-butadiene to the living PS a very minor fraction of the PS chains has coupled, resulting in a weak shoulder

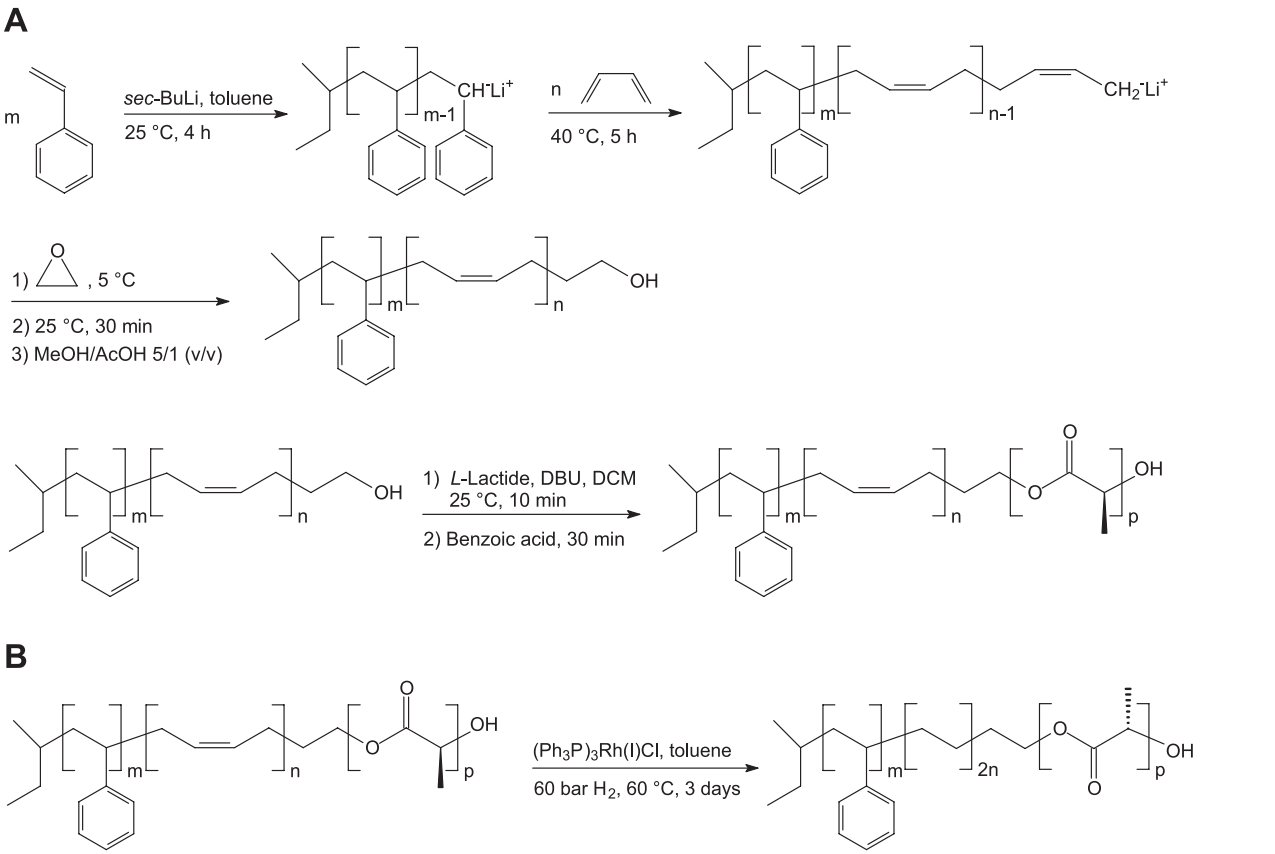

SCHEME 2 | (A) Synthesis of SBL triblock terpolymers by combination of living anionic polymerization and organo-catalyzed ROP of *L*-lactide, followed by (B) catalytic hydrogenation to yield the respective SEL triblock terpolymers.

TABLE 1 | Molecular characteristics of the employed triblock terpolymers and the SB-OH diblock copolymer precursor.

Sample[a,b]	Code	$\overline{M}_n$(PB)[c] / $\overline{M}_n$ (PE) [g mol^{-1}]	$\overline{M}_n$(*PLLA*)[c] [g mol^{-1}]	$\overline{M}_{n,total}$ [g mol^{-1}]	$Đ$[d]	1,4-PB/Ethyl[e] [mol-%]
$S_{296}B_{312}$-OH	SB-OH	16,900	—	47,700	1.06	89/–
$S_{296}B_{312}L_{368}$	SBL-1	16,900	26,500	74,200	1.24	89/–
$S_{296}B_{312}L_{781}$	SBL-2	16,900	56,300	104,000	1.10	89/–
$S_{296}E_{590}L_{368}$	SEL-1	17,500	26,500	74,800	—	–/5.8
$S_{296}E_{590}L_{781}$	SEL-2	17,500	56,300	104,600	—	–/5.8

[a]Indices give the number-average degree of polymerization of the respective block; for *PLLA* the number corresponds to lactic acid repeating units.
[b]$\overline{M}_n$(PS) = 30,800 g mol^{-1}, as determined by matrix-assisted laser desorption/ionization time-of-flight (MALDI-ToF) mass spectrometry (Figure S1A).
[c]Determined by ^{1}H NMR using $\overline{M}_n$(PS) (from MALDI-ToF) for internal signal calibration.
[d]Determined by $CHCl_3$-SEC employing a PS calibration.
[e]1,4-PB: Average mole fraction of 1,4-PB units determined by ^{1}H NMR; Ethyl: Average mole fraction of ethyl branches in the PE block calculated from the mole fraction of 1,4-PB units in the respective SBL triblock terpolymer precursor.

in the distributions of SB-OH and SBL-2 at lower molecular weights.

In the next step, the PB middle block of the SBL triblock terpolymers was hydrogenated employing Wilkinson's catalyst to yield SEL triblock terpolymers with a crystallizable PE middle block (Scheme 2B) [81]. Complete hydrogenation of the PB middle blocks to PE was proven by proton nuclear magnetic resonance (^{1}H NMR) spectroscopy by the absence of PB specific signals after hydrogenation (Figure 1B, Figure S1C). In addition, differential scanning calorimetry (DSC) on bulk samples revealed melting transitions specific for PE and *PLLA*, showing that both blocks are able to crystallize (Figure S2).

2.2 | CDSA in a Good Solvent for the PS and *PLLA* Corona Blocks

CDSA was first studied in THF, a good solvent for both corona blocks (PS and *PLLA*). The optimum crystallization conditions

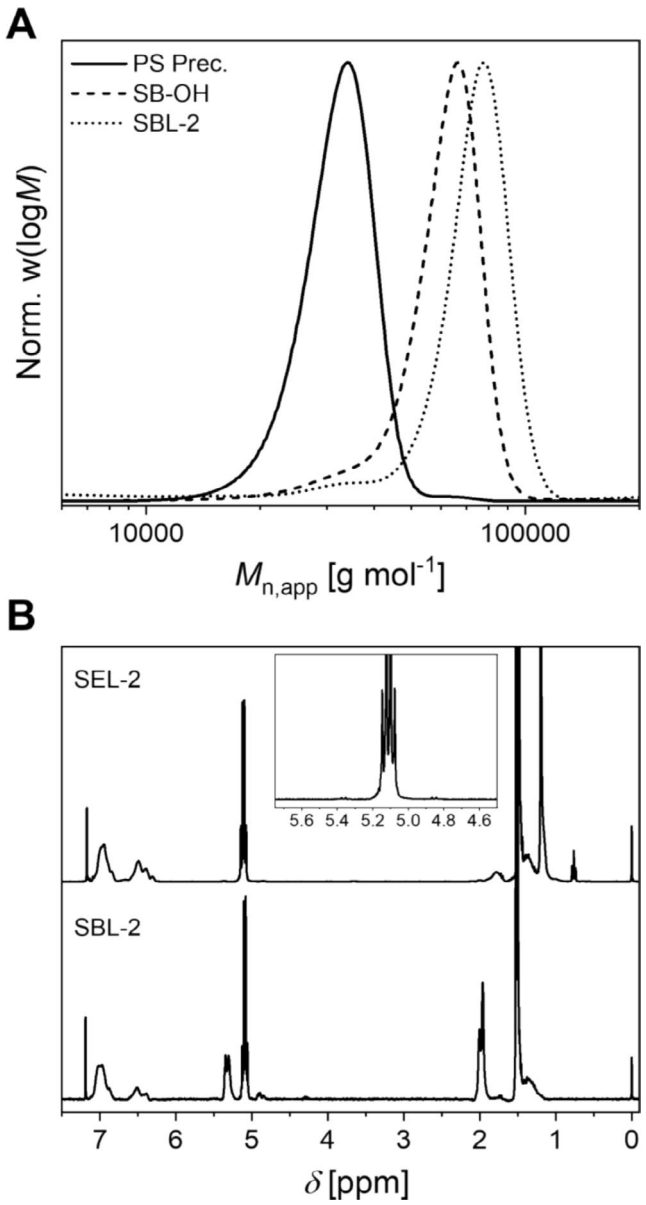

FIGURE 1 | (A) Apparent molecular weight distributions of SBL-2 and the respective PS and SB-OH precursors ($CHCl_3$-SEC, PS calibration). (B) ^{1}H NMR spectra (in $CDCl_3$) of SBL-2 and SEL-2 (measured at 60°C) proving complete hydrogenation by lack of PB specific signals (δ = 5.4–5.2, 4.9–4.8, and 2.1–1.9 ppm) in SEL-2.

for the PE middle block were probed by micro-DSC (μ-DSC) measurements for SEL-1 and SEL-2 at a concentration of $c = 10\,g\,L^{-1}$ in THF (Figure 2A,B). The employed temperature profile is depicted in Figure S3.

For both SEL triblock terpolymers rather broad crystallization and melting transitions can be observed for the PE middle block (T_c (PE) ≈ 30°C–32°C, T_m (PE) ≈ 50°C–52°C, Table S1). For SEL-1 it seems that the crystallization exotherm is composed of two unresolved underlying exotherms. However, this effect was not observed for the other solvents employed in this study (Figure 3B). Rather broad thermal transitions are typical for pseudo PE blocks due to the presence of ethyl branches (5.8 mol-% on average), arising from the 11 mol-% 1,2-units in the respective PB precursor block (Table 1) [40, 52]. Due to a certain nonuniformity in the distribution of the branches within the PE chains a distribution of melting and crystallization temperatures results. Melting or crystallization transitions for the PLLA blocks are not discernable. This is in accordance with THF being a good solvent for PLLA, whereas the pseudo PE block is only soluble in THF above its melting point at elevated temperatures [52].

Accordingly, the SEL triblock terpolymers were first dissolved in THF at 65°C for 10 min, followed by cooling to the peak crystallization temperature (T_c) of the PE middle block (T_c (PE) = 30 and 32°C for SEL-1 and SEL-2, respectively) to initiate CDSA. After isothermal crystallization for 24 h, the solutions were slowly cooled to −10°C to enable crystallization of the PE chains with a higher fraction of ethyl branches, that is, lower crystallization temperature. A detailed description of the CDSA procedure can be found in Section 4. The morphology of the formed micelles was then examined by transmission electron microscopy (TEM), employing selective staining of PS with ruthenium tetroxide (RuO_4). Figure 2C,D reveals that wCCMs with bright appearing, semi-crystalline PE cores were formed for both SEL triblock terpolymers. The formation of wCCMs is consistent with our prior work on CDSA of polystyrene-*block*-polyethylene-*block*-poly(methyl methacrylate) triblock terpolymers [52]. This study showed that wCCMs are formed in good solvents for PE, being able to molecularly dissolve the PE block at elevated temperatures, like THF or toluene. The occurrence of branches and kinks in the semi-crystalline PE core is induced by the ethyl branches in the PE block, which are formed after hydrogenation of the 1,2-PB repeating units (Table 1) [52, 81]. The corona of the wCCMs appears dark due to the selective staining of the PS chains and shows a patch-like structure with embedded, bright appearing PLLA patches (not stained). The microphase-separated structure of the corona arises from the moderate incompatibility of the PS and PLLA corona chains with a Flory-Huggins interaction parameter of $\chi = 0.15$ at 110°C [82], that is, similar to the behavior observed for wCCMs with a patch-like PS/PMMA corona [52, 81, 83]. As PLLA is prone to partial electron beam degradation, the size of the PLLA patches might be somewhat underestimated from the TEM micrographs. The patchy SEL wCCMs have a strong tendency to agglomerate, which is an artifact from TEM sample preparation. Agglomeration of the wCCMs occurs upon drying on the carbon-coated TEM grid, an effect that has also been observed for other patchy wCCMs [40, 49, 52, 83].

2.3 | CDSA in Selective Solvents for the PS Corona Block

To probe whether the PLLA blocks in the patchy wCCM corona are able to crystallize and how PLLA crystallization influences the corona structure, CDSA was conducted in solvents or solvent mixtures with decreasing solvent quality for PLLA, that is, xylene (Xyl, isomeric mixture) and mixtures with cyclohexane (CH, up to 30 vol-%). In contrast to PS, the PLLA homopolymer is insoluble in Xyl or Xyl/CH mixtures at room temperature. Only upon heating to temperatures $T > 65$°C does PLLA become soluble, as probed by solubility tests with a $PLLA_{152}$ homopolymer.

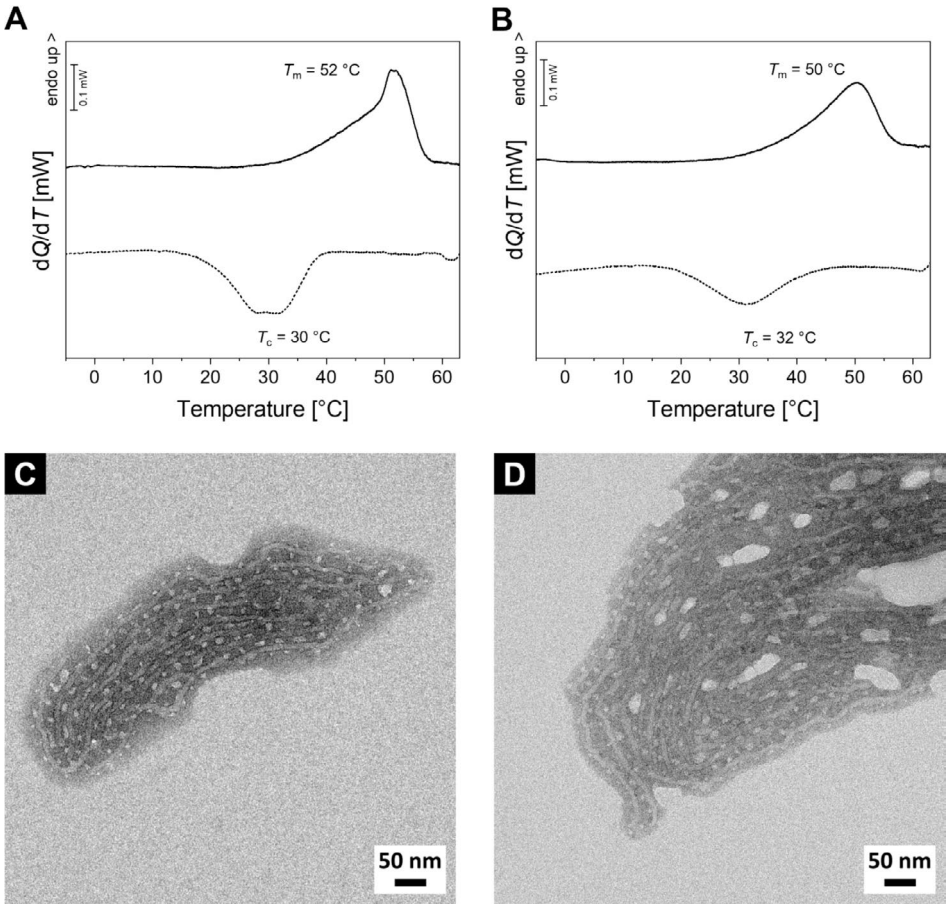

FIGURE 2 | μ-DSC heating and cooling traces for (A) SEL-1 and (B) SEL-2 in THF at $c = 10\,g\,L^{-1}$ (scanning rate: $0.5\,K\,min^{-1}$). TEM micrographs of wCCMs formed by CDSA of (C) SEL-1 and (D) SEL-2 in THF. PS was selectively stained with RuO_4 and appears dark.

Figure 3A,B shows the μ-DSC heating and cooling traces for SEL-1 in Xyl, and Xyl/CH mixtures with 20 and 30 vol-% CH, respectively ($c = 10\,g\,L^{-1}$). The μ-DSC traces for SEL-1 in Xyl are comparable to the results obtained for THF as solvent. In both cases, crystallization and melting can only be observed for the PE middle block, whereby the peak melting temperature is slightly reduced to T_m (PE) $\approx$ 48°C in Xyl (Table S1). This might be attributed to Xyl being a slightly better solvent for PE at elevated temperatures, resulting in a more pronounced plasticizing effect. Here, it has to be noted that stainless steel batch cells sealed with fluororubber (FKM) O-rings were employed for μ-DSC measurements. The limited "inertness" of the fluororubber against Xyl and CH gives rise to artifact peaks in the cooling (endothermic peaks) and heating (exothermic peaks) traces for temperatures below ca. 10°C (Figure S4). Hence, in this temperature range visible transitions were not considered. Similar observations were reported when chloroform was used as solvent [84].

In the Xyl/CH = 80/20 (v/v) mixture an additional weak endotherm appears in the heating trace at T_m = 33°C, which gets more pronounced and shifts to higher temperatures (T_m = 36°C) upon increasing the CH content to 30 vol-% (Figure 3A, Table S1). Hence, these endotherms can be assigned to the melting of PLLA within the patch-like SEL-1 wCCM corona. In the respective cooling traces (Figure 3B) crystallization can only be detected for the Xyl/CH = 70/30 (v/v) mixture (T_c (PLLA) = 15°C), suggesting that for 20 vol-% CH crystallization of PLLA can either be not resolved or occurs during the isotherm at −15°C. The PLLA melting and crystallization temperatures are significantly reduced compared to that in the respective bulk sample (Figure S2), which can be attributed to a plasticizing effect of the used solvents. The estimated degrees of crystallinity for PLLA are in both mixtures well below α = 5% (Table S1). Hence, crystallization appears to be significantly hampered by the confinement imposed by the patchy corona structure. For the PE middle block, the corresponding crystallization and melting transitions are again rather broad and slightly shifted to lower temperatures in the Xyl/CH mixtures (T_c (PE) = 27°C, T_m (PE) $\approx$ 44°C–45°C), which is attributed to the more pronounced plasticizing effect of CH.

For SEL-2 (Figure 3C,D) melting of PLLA could already be detected in pure Xyl, with the respective heating trace showing multiple weak endothermic peaks attributable to PLLA (first most intense endotherm at T_m (PLLA) = 44°C, Table S1). This might be ascribed to the increased length of the PLLA block in SEL-2, resulting in a reduced solubility in pure Xyl. The observed multiple PLLA endotherms might be attributed either to the patchy structure of the corona, resulting in crystals of different thickness and/or perfection, or to rearrangement processes upon heating. The PE block shows a rather broad melting transition (T_m (PE) $\approx$ 48°C) being superimposed with

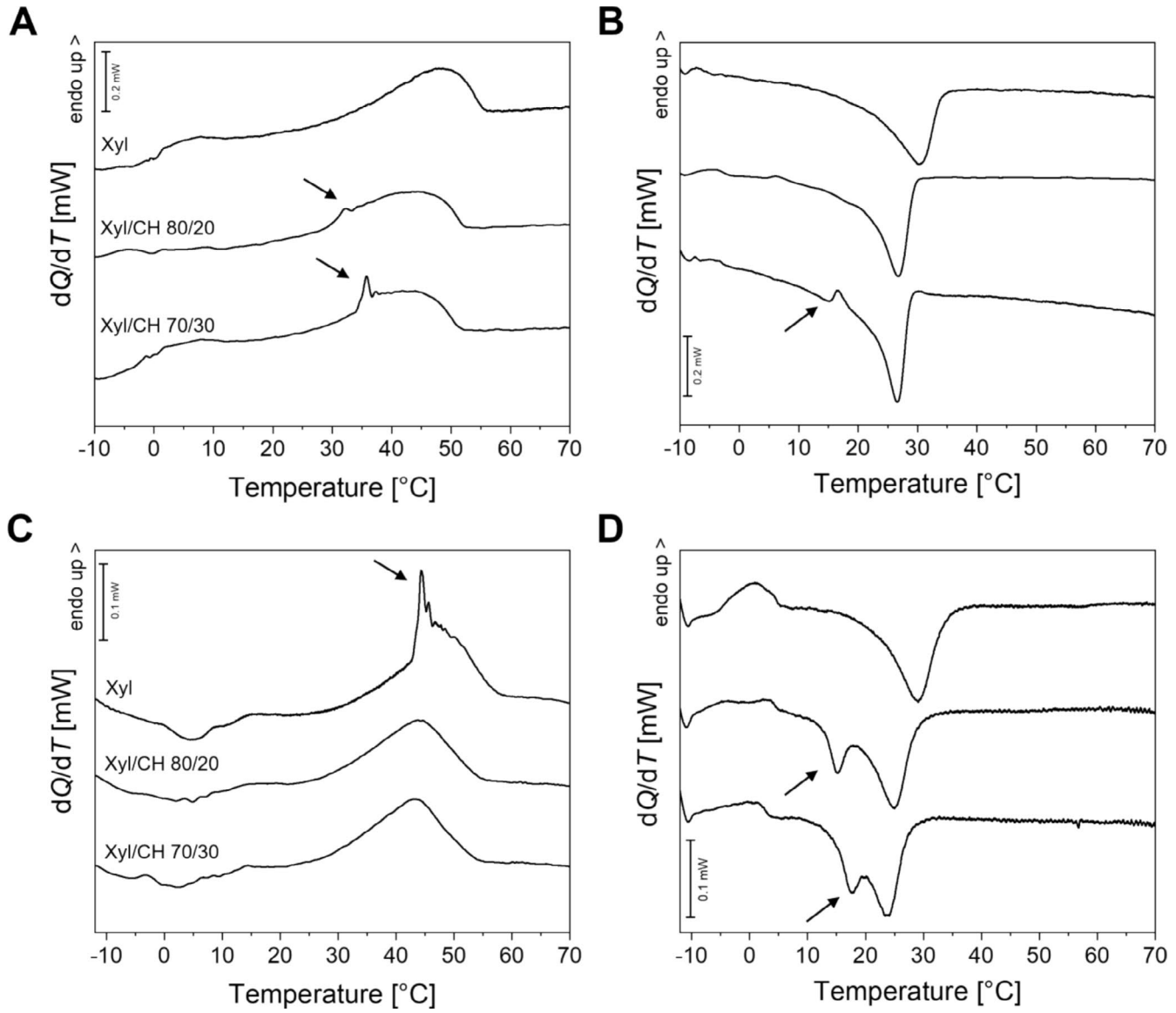

FIGURE 3 | μ-DSC heating and cooling traces for (A, B) SEL-1 and (C, D) SEL-2 in Xyl, Xyl/CH = 80/20 (v/v) and Xyl/CH = 70/30 (v/v) ($c = 10\,g\,L^{-1}$, scanning rate: $0.5\,K\,min^{-1}$). Arrows indicate melting and crystallization transitions of the P*L*LA block.

the P*L*LA endotherms. In the respective cooling trace, only one exotherm attributable to PE crystallization can be detected (T_c (PE) = 29°C), implying that P*L*LA crystallization took place during the isothermal at −15°C. In contrast to SEL-1, clear P*L*LA crystallization exotherms are discernible in the cooling traces of SEL-2 in Xyl/CH mixtures. The respective crystallization temperatures increase with the CH content from T_c (P*L*LA) = 15°C (20 vol-% CH) to T_c (P*L*LA) = 18°C (30 vol-% CH), whereby the degree of crystallinity is still below 5% despite the significantly higher P*L*LA content in SEL-2 (Table S1). In the heating traces, only one broad melting transition can be observed for both Xyl/CH mixtures, which might result from comparable melting points and, accordingly, strongly overlapping PE and P*L*LA endotherms. It is noted that the "apparent" degree of crystallinity for the PE block calculated from the heating traces (α_{app} (PE) = 40%–43%) is significantly higher compared to the degree of crystallinity obtained from the respective cooling traces (α (PE) = 33%), where PE and P*L*LA crystallization exotherms can be separated. An effect that was not observed for SEL-1 in Xyl, where only the PE block was able to crystallize with α (PE) = 64% and 65%, as determined from the cooling and heating traces, respectively. This underlines the assumption that P*L*LA melting is "hidden" due to a strong overlap of PE and P*L*LA endotherms and, hence, the "apparent" degree of crystallinity derived from the heating traces is higher.

We have selected the Xyl/CH = 80/20 (v/v) mixture for further CDSA experiments and morphological studies. In pure Xyl crystallization of the P*L*LA block was only observed for SEL-2. Besides, for the mixture with 30 vol-% CH the P*L*LA crystallization exotherm strongly overlaps with the PE exotherm for SEL-2, that is, both blocks partially crystallize at the same time upon cooling. Hence, for the Xyl/CH = 80/20 (v/v) mixture the P*L*LA blocks are able to crystallize for both SEL triblock terpolymers and the PE and P*L*LA crystallization exotherms are sufficiently separated by 10°C for SEL-2. Nevertheless, for both SEL triblock terpolymers the fraction

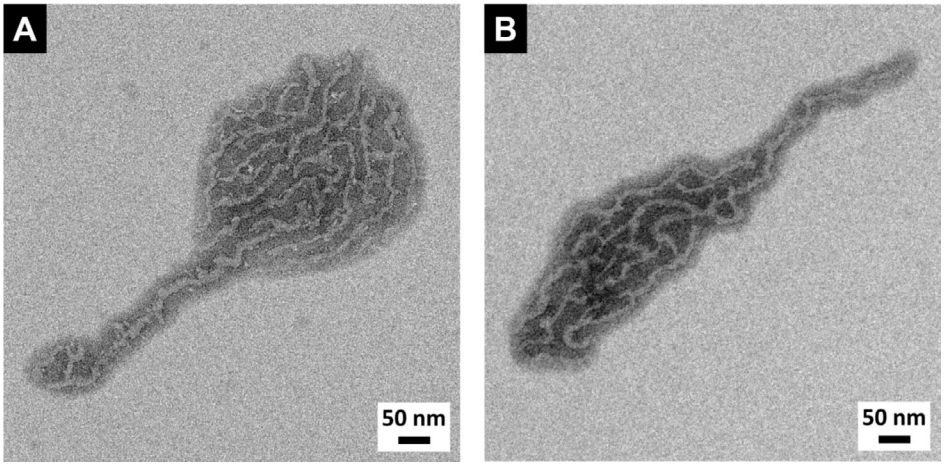

FIGURE 4 | TEM micrographs of wCCMs formed by CDSA of (A) SEL-1 and (B) SEL-2 in Xyl/CH = 80/20 (v/v) mixture. PS was selectively stained with RuO_4 and appears dark.

of crystalline P*L*LA is very low (α (PLLA) ≤ 3%, Table S1). CDSA was conducted analogously to the procedure described for wCCMs prepared in THF, except that the dispersions were initially heated to 80°C. The employed peak crystallization temperatures for the PE block are listed in Table S1. Figure 4 shows the respective TEM micrographs of the structures formed by CDSA of SEL-1 and SEL-2 in Xyl/CH = 80/20 (v/v), using again selective staining with RuO_4.

The formation of worm-like micelles with a bright appearing PE core can be clearly deduced for both SEL triblock terpolymers. However, in contrast to the wCCMs formed in THF (Figure 2C,D), the P*L*LA patches are difficult to identify. The corona of the wCCMs appears dark due to the selective staining of the PS blocks and there are only a few small, bright appearing P*L*LA patches discernable. This might be attributed to the limited solubility of the P*L*LA corona blocks in the Xyl/CH mixture, resulting in a pronounced shrinkage/collapse of the P*L*LA patches. Accordingly, the collapsed P*L*LA patches decrease in size and will be located closer to the likewise bright appearing PE cores, which makes their detection difficult. A similar effect of decreasing patch sizes was observed for wCCMs with a patch-like PS/PMMA corona prepared in toluene, being a slightly better solvent for the PS corona blocks [52]. Moreover, the PE cores of the wCCMs shown in Figure 4 exhibit a pronounced undulated structure, which was not visible for the wCCMs prepared in THF. This supports the assumption of collapsed P*L*LA patches being located close to the PE cores.

The studies in Xyl and Xyl/CH mixtures reveal that crystallization of the P*L*LA block within the patch-like microphase-separated PS/P*L*LA corona is possible when the solvent quality for the P*L*LA block is reduced. However, in contrast to our prior results on CDSA of a PS-*b*-PE-*b*-PEO (SEEO) triblock terpolymer [54], which forms wCCMs with a Janus-type PS/PEO corona, crystallization is hindered due to the confinement exerted by the patchy corona structure. The latter results in strongly decreased degrees of crystallinity for the P*L*LA blocks in the patchy SEL wCCMs (α (P*L*LA) < 5%). In contrast, a significantly higher degree of crystallinity was found for the PEO block in Janus-type SEEO wCCMs (α (PEO) = 63%).

2.4 | SCDSA of Patchy SEL wCCMs With P*D*LA Homopolymer

In our previous work, we have shown that SCDSA of diblock copolymer mixtures bearing enantiomeric P*L*LA and P*D*LA blocks can be utilized to form well-defined micelles with a semi-crystalline P*L*LA/P*D*LA SC core in non-solvents for the polylactide SC [78, 79]. Accordingly, using a similar approach, it should be possible to selectively load the P*L*LA patches in the corona of patchy SEL wCCMs driven by stereocomplexation with an enantiomeric P*D*LA homopolymer. This might be harnessed to add further functionality to the wCCMs, like fluorescence. To test this concept, a SEL-1 wCCM dispersion in Xyl/CH = 80/20 (v/v) was used ($c = 10\,g\,L^{-1}$). The solubility of the P*L*LA blocks in the corona patches is sufficiently limited in this solvent mixture, indicated by the ability of the P*L*LA blocks to crystallize (Figure 3A, Table S1). This limited solubility should also promote SC formation. Importantly, the degree of crystallinity for P*L*LA in the patches is sufficiently low (α (P*L*LA) ≈ 2%) and, hence, should not impair SC formation. SCDSA was induced by adding a solution of $PDLA_{62}$ homopolymer in THF ($c = 10\,g\,L^{-1}$) to the wCCM dispersion at a ratio of P*L*LA/P*D*LA units of 2/1 (w/w). A $PDLA_{62}$ homopolymer with a lower degree of polymerization with respect to the P*L*LA block in SEL-1 ($S_{296}E_{590}L_{368}$) and an excess of P*L*LA units were deliberately chosen to avoid a possible cross-linking of the wCCMs during SC formation. The mixture was then aged for 7 days without stirring, and the added THF was allowed to evaporate to facilitate SC formation. First, SC formation was probed by TEM (Figure 5). From the micrograph, it becomes evident that the overall worm-like structure of the micelles was preserved, with the PE cores again appearing bright (not stained by RuO_4). Also, cross-linking of micelles seems not to be a major issue, as the observed partial agglomeration is very similar to that observed for neat SEL-1 wCCMs (Figures 2C and 4A). In contrast, more globular assemblies might be expected in case of pronounced cross-linking.

Notably, the corona structure differs distinctly from that of SEL-1 wCCMs prepared in THF (Figure 2C) and Xyl/CH = 80/20 (v/v) (Figure 4A). The bright patches are

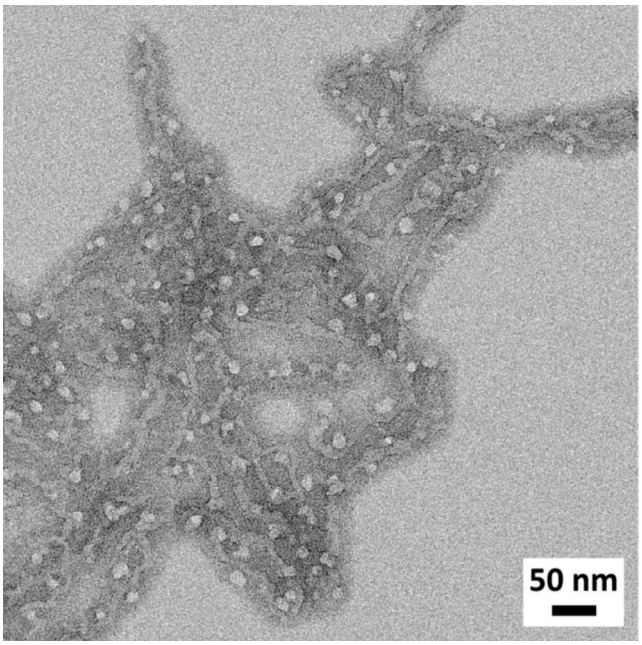

FIGURE 5 | TEM micrograph of wCCMs with SC patches prepared by SCDSA of SEL-1 wCCMs with P*D*LA$_{62}$ homopolymer in a Xyl/CH = 80/20 (v/v) mixture. PS was selectively stained with RuO_4 and appears dark.

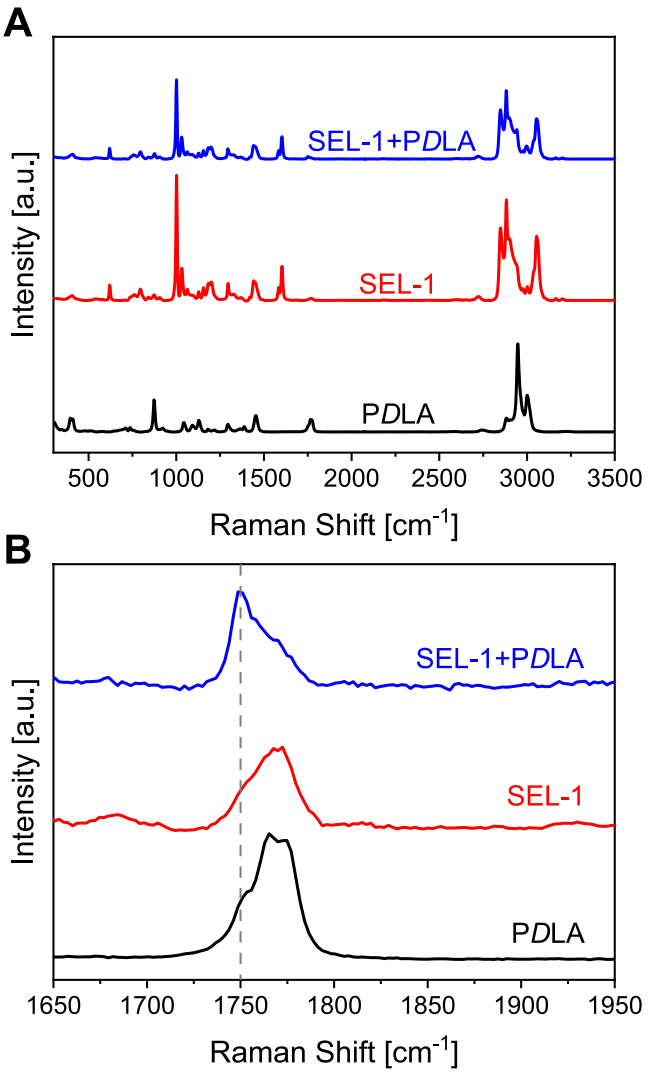

FIGURE 6 | Raman spectra of PDLA$_{62}$ homopolymer and dried SEL-1 wCCM dispersions before and after SCDSA with P*D*LA$_{62}$. (A) Full spectra and (B) zoom-ins of the carbonyl stretching vibration regime (dashed line indicates location of SC specific band).

significantly larger and exhibit a square-like shape. They are embedded in the dark appearing PS corona (selectively stained with RuO_4), shielding the insoluble SC patches. In addition, RuO_4 is also known to preferentially stain interfaces, which results in the appearance of a darker ring around the SC patches. The area of the P*L*LA/P*D*LA SC patches, as obtained from TEM image analysis (Figure S5), is with $135 \pm 40\,nm^2$ about twice the area of the P*L*LA patches of neat SEL-1 wCCMs in THF ($73 \pm 26\,nm^2$). In comparison, the P*L*LA patches were very small and hard to identify for the corresponding neat SEL-1 wCCMs in Xyl/CH = 80/20 (v/v). Hence, the significant increase in size is a strong indication of successful SC formation within the patchy wCCM corona.

SC formation can be proven by infrared or Raman spectroscopy by a characteristic shift of the carbonyl stretching vibration of P*L*LA or P*D*LA to lower wavenumbers upon stereocomplexation [85, 86]. Figure 6 compares the Raman spectra of the employed P*D*LA$_{62}$ homopolymer and dried SEL-1 wCCM dispersions before and after stereocomplexation. The carbonyl stretching band shifts from $\tilde{\nu} \approx 1768\,cm^{-1}$ for P*D*LA$_{62}$ and neat SEL-1 wCCMs to $\tilde{\nu} \approx 1750\,cm^{-1}$ for the SEL-1 + P*D*LA$_{62}$ SC wCCMs, proving the formation of SC patches in the wCCM corona. As the employed ratio of P*L*LA/P*D*LA units was 2/1 (w/w), the carbonyl band does not completely shift to lower wavenumbers, as there is still an excess of P*L*LA units in the patches that did not take part in stereocomplexation.

Interestingly, when using the identical approach for SCDSA of P*D*LA$_{62}$ with SEL-2 wCCMs, SC formation was not successful. In the respective TEM micrographs (Figure S6) large platelet-like structures are visible that most likely consist of P*D*LA homopolymer that crystallized upon drying the mixture on the TEM grid. In addition, the corona of the wCMMs shows hardly any patches, which is comparable to the structure found for neat SEL-2 wCCMs in Xyl/CH = 80/20 (v/v) (Figure 4B). The different behavior of SEL-2 ($S_{296}E_{590}L_{781}$) might be attributed to the significantly longer P*L*LA corona block, with a degree of polymerization about twice as high as for SEL-1 ($S_{296}E_{590}L_{368}$). Accordingly, the solubility of the longer P*L*LA blocks in Xyl/CH = 80/20 (v/v) is even more reduced and hinders efficient SC formation under the employed conditions.

2.5 | Stereocomplex-Driven Fluorescence Labeling of Patchy SEL wCCMs

We utilized SCDSA to selectively introduce a fluorescent dye into the P*L*LA patches of SEL-1 wCCMs. This not only allows selective functionalization of the P*L*LA patches but also provides an elegant method to detect SC formation directly in the dispersion using fluorescence correlation spectroscopy (FCS). To this end, a rhodamine B end-functionalized P*D*LA homopolymer (P*D*LA$_{62}$-RB, details on synthesis are provided

in the Section 4) was synthesized, and SCDSA was performed in an identical manner as described above. TEM reveals a basically identical morphology for the fluorescently labeled SEL-1 + P*D*LA$_{62}$-RB SC wCCMs (Figure S7) as compared to that of the non-labeled SC wCCMs (Figure 5). This shows that SCDSA is not altered by the presence of the fluorescent dye at the P*D*LA chain end.

FCS was then used to study the diffusion of the single dye-labeled polymer chains in highly diluted solutions [87], thus providing a tool to distinguish between molecularly dissolved P*D*LA$_{62}$-RB or P*D*LA$_{62}$-RB immobilized in the patches of wCCMs by stereocomplexation. According to the Stokes-Einstein relation, the diffusion coefficient is inversely proportional to the hydrodynamic radius. The significantly larger size of SC wCCMs compared to single P*D*LA$_{62}$-RB chains translates to a much larger hydrodynamic radius. Consequently, substantially reduced diffusion coefficients are expected for the SC wCCMs, leading to longer diffusion times observable in FCS measurements. Figure 7 compares the normalized autocorrelation of intensity data for P*D*LA$_{62}$-RB in THF (molecularly dissolved) and SEL-1 + P*D*LA$_{62}$-RB SC wCCMs in Xyl/CH = 80/20 (v/v). The results reveal that the correlation time of the P*D*LA$_{62}$-RB chains is about 3 orders of magnitude shorter than that of the micelles. This observation aligns with the expectation that micelles diffuse much more slowly. Notably, the autocorrelation data for the SEL-1 + P*D*LA$_{62}$-RB SC wCCMs exhibit no multi-step descent in the curve, indicating the absence of freely diffusing individual P*D*LA$_{62}$-RB chains or significantly larger structures that might have been formed by homo-crystallization of non-complexed P*D*LA$_{62}$-RB. Hence, in agreement with the TEM and Raman spectroscopy results discussed above, FCS confirms successful SC formation within the patches of the SEL-1 wCCMs. The important difference between the methods is that FCS can directly detect SC formation in the dispersion, whereas TEM or Raman spectroscopy can only examine the samples in the dried state.

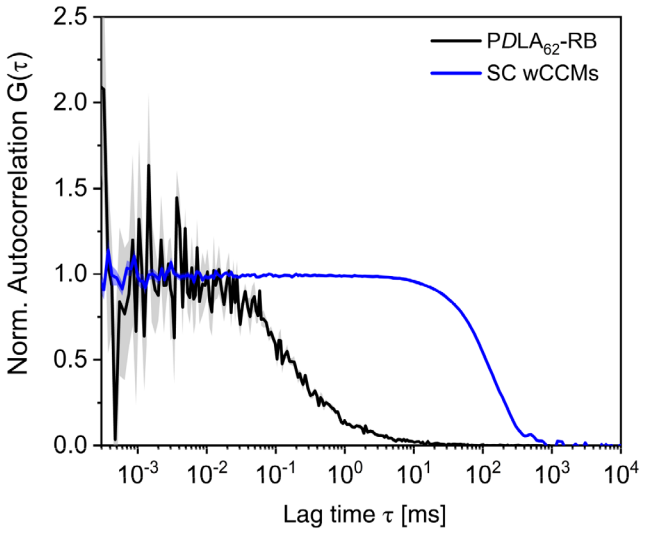

FIGURE 7 | FCS autocorrelation of intensity data of P*D*LA$_{62}$-RB homopolymer in THF ($c = 1 \cdot 10^{-8}$ g L^{-1}) and SEL-1 + P*D*LA$_{62}$-RB SC wCCMs in Xyl/CH = 80/20 (v/v) ($c = 1$ g L^{-1}). Errors are displayed as transparent areas.

3 | Conclusion

This work shows that well-defined patchy wCCMs can be prepared by CDSA of double-crystalline polystyrene-*block*-polyethylene-*block*-poly(*L*-lactide) (PS-*b*-PE-*b*-P*L*LA) triblock terpolymers. CDSA to patchy wCCMs is driven by the crystallization of the PE middle block due to its insolubility in common organic solvents at room temperature. In THF, being a good solvent for the PS and P*L*LA corona blocks, only crystallization of the PE block is observed, resulting in wCCMs with an amorphous patchy PS/P*L*LA corona. However, when the solvent quality for the P*L*LA block is sufficiently reduced, for example, in xylene or xylene/cyclohexane mixtures, crystallization within the P*L*LA patches is induced without compromising the overall shape of the patchy wCCMs. Furthermore, the stereoregular P*L*LA patches can be selectively loaded by stereocomplexation with enantiomeric P*D*LA homopolymers, yielding wCCMs with P*L*LA/P*D*LA SC patches in the corona. In this way, also further functionalities can be introduced in the patchy corona as exemplified with a fluorescently labeled P*D*LA homopolymer. This in turn presents an elegant way to follow stereocomplexation directly in dispersion employing fluorescence correlation spectroscopy. Here, a clear shift of the autocorrelation of intensity data to longer correlation times proves the successful incorporation of the P*D*LA chains into the larger, slower diffusing wCCMs.

In future research, the concept of stereocomplex-driven loading can be harnessed to incorporate different (functional) guest molecules or nanoparticles into the corona of wCCMs with stereoregular P*L*LA patches. In addition, employing block copolymers or micelles with enantiomeric P*D*LA blocks/coronas might enable the construction of hierarchically structured micellar assemblies. As the efficiency of stereocomplexation is highly dependent on the employed solvent and/or temperature, access to dynamic assemblies might also be envisaged.

4 | Experimental Section

4.1 | Materials

All chemicals were used as received unless otherwise noted. Ethylene oxide (Linde, 3.0) was stirred over calcium hydride (CaH_2) at 0°C for 3 h before being transferred into a storage ampoule. Prior to use, ethylene oxide was additionally purified over *n*-butyllithium (*n*-BuLi) at 0°C. 1,3-Butadiene (2.5, Tyczka Industrie-Gase GmbH) was passed over columns with molecular sieves and activated alumina, followed by storage over di-*n*-butylmagnesium (Bu_2Mg) before use. Styrene (> 99%, Sigma-Aldrich) was stirred over Bu_2Mg under nitrogen and condensed into a storage ampoule. Dichloromethane (DCM, ≥ 99.8% stabilized with amylene, analytical reagent grade, Thermo Scientific) used for lactide polymerization was dried by distillation over CaH_2. Toluene (technical grade) for anionic polymerization was purified over 1,1-diphenyl-3-methylpentyllithium, prepared in situ by the reaction of *sec*-butyllithium (*sec*-BuLi) with 1,1-diphenylethylene (DPE), refluxed for 2–3 days under dry nitrogen, and distilled directly before use. 1,8-Diazabicyclo[5.4.0]undec-7-ene (DBU, > 98%, TCI) was dried by distillation over CaH_2. *D*- and *L*-lactide (≥ 99.8%, PURASORB D and L, Corbion, Amsterdam, The Netherlands)

were recrystallized from toluene and stored under argon until use. DPE (> 98%, TCI) was stirred with *sec*-BuLi under argon atmosphere, distilled under vacuum, and stored under argon until use. Pyridine (> 99%, Carl Roth) was dried successively over KOH and CaH_2 and distilled prior to use. Sulforhodamine B acid chloride (pure, Thermo Scientific), Bu_2Mg (1.0 M in heptane, Sigma-Aldrich), *sec*-BuLi (1.3 M in cyclohexane/hexane, Thermo Scientific), *n*-BuLi (1.6 M in hexanes, Thermo Scientific), benzoic acid (p.a., AlppiChem), 2-hydroxyethyl 2-bromo*iso*butyrate (HEB*i*B, 95%, Sigma-Aldrich), *trans*-2-[3-(4-*tert*-butylphenyl)-2-methyl-2-propenylidene]malononitrile (DCTB, HPLC grade, Sigma-Aldrich), silver trifluoroacetate (AgTFA, > 99.9%, Sigma-Aldrich), deuterated chloroform ($CDCl_3$, 99.8%, Deutero), tris(triphenylphosphine)rhodium(I) chloride (Wilkinson's catalyst, ≥ 99.9%, Sigma-Aldrich), ruthenium(III) chloride hydrate (ReagentPlus, Sigma-Aldrich), sodium hypochlorite solution (NaOCl, 10–15 wt% in water, Thermo Scientific), acetic acid (≥ 99.7%, analytical reagent grade, Thermo Scientific), hydrochloric acid (37%, Thermo Scientific), xylene (Xyl, 99.5%, isomeric mixture, Grüssing GmbH), cyclohexane (CH, ≥ 99.8%, analytical reagent grade, Thermo Scientific), acetone (≥ 99.5%, puriss. p.a., ACS reagent, Sigma-Aldrich), 2-propanol (≥ 99.8%, puriss. p.a., ACS reagent, Sigma-Aldrich), toluene (≥ 99.5%, AnalaR NORMAPUR ACS, Reag. Ph. Eur., VWR chemicals) and methanol (MeOH, ≥ 99.9%, analytical reagent grade, Thermo Scientific).

4.2 | Methods

^1H NMR spectroscopy was carried out with a Bruker Ultrashield-300 spectrometer (300 MHz) at 20 or 60°C in the case of SEL triblock terpolymers. The chemical shift (δ) was determined relative to the residual solvent signal of $CDCl_3$ (δ (^1H) = 7.26 ppm).

SEC was conducted with an Agilent 1200 Infinity system (Agilent Technologies, Santa Clara, CA, USA) equipped with an SDV gel precolumn (particle size = 5 μm, PSS, Mainz, Germany) and an SDV linear XL gel column (particle size = 5 μm) with a porosity range from 10^2 to 10^5 Å (PSS, Mainz, Germany) using $CHCl_3$ (HPLC grade) as the eluent. The samples were measured at a flow rate of 0.5 mL min^{-1} at 23°C, and a refractive index (RI) detector (1260 Infinity, Agilent Technologies, Santa Clara, CA, USA) was used. Prior to analyses, all samples were dissolved and filtered through a 0.2 μm PTFE filter. The SEC system was calibrated with narrowly distributed PS standards (PSS calibration kit) and toluene (HPLC grade) was used as the internal standard.

Matrix-assisted laser desorption/ionization time-of-flight mass spectrometry was performed with a Bruker Daltonics autoflex maX (Bruker, Germany) equipped with a smartbeam-II solid state laser and operating in linear mode. The samples were prepared by the dried droplet method using DCTB as matrix and AgTFA as ionization agent. All components were dissolved in THF (HPLC grade) at a concentration of $c = 10$ g L^{-1} and mixed together in a volumetric ratio of matrix/sample/ionization agent = 20/5/1.

DSC of the bulk samples was performed on a Phoenix 204 F1 (Netzsch, Selb, Germany) using aluminum crucibles with pierced lids. Measurements were done under a nitrogen atmosphere within a temperature range of −50 to 200°C (scanning rate of 10 K min^{-1}).

μ-DSC was conducted with a Setaram μDSC III at a scanning rate of 0.5 K min^{-1}. The samples ($c = 10$ g L^{-1}) were dissolved at 60°C (for THF) or 70°C (for Xyl and Xyl/CH mixtures) for 1 h and transferred into closed "batch" cells sealed with fluororubber (FKM) O-rings. The pure solvent or solvent mixture was used as a reference.

Raman spectroscopy was carried out on a confocal WITec Alpha 300 RA+ Raman imaging system equipped with a UHTS 300 spectrometer and a back-illuminated Andor Newton 970 EMCCD camera (WITec Suite SIX 6.1 software package). Raman spectra of the dried micelle dispersions and the P*D*LA homopolymer were acquired with an excitation wavelength of $\lambda = 532$ nm and a 100x objective (Zeiss EC Epiplan-Neofluar DIC, $NA = 0.9$), employing a laser intensity of 20 mW and an integration time of 0.5 s (50–100 accumulations). All spectra were corrected for cosmic ray spikes and subjected to a background removal routine. Samples of the micelle dispersions were prepared by dropping small amounts (3 × 10 μL) of the dispersion onto a glass slide followed by drying in vacuo (24 h, 20 mbar).

FCS was performed on a commercial confocal microscope MicroTime 200 (PicoQuant). For excitation of the Rhodamine B dyes attached to the P*D*LA chains, a laser diode with a wavelength of $\lambda = 560$ nm (LDH-D-TA-560B, PicoQuant) operated in pulsed mode with a repetition rate of 20 MHz was used. The excitation intensities were adjusted to approximately 1010 W cm^{-2} for P*D*LA$_{62}$-RB in THF and 8.8 W cm^{-2} for the SEL-1 + P*D*LA$_{62}$-RB SC wCCMs in Xyl/CH = 80/20 (v/v). Radiation from the laser was directed through a single-mode optical fiber into the main optical unit, reflected by a dichroic mirror (ZT488/561rpc, AHF/Chroma) into an inverted confocal optical microscope (Olympus IX73), and focused into a quartz cuvette using a semi-apochromatic objective (LUCPLFLN60X, $NA = 0.7$, Olympus) with a long working distance (1.5—2.2 mm). The signal from the sample was transmitted to the dichroic mirror and passed through a long pass filter (561 LP Edge Basic, Semrock). The signal was detected by a single-photon counting avalanche diode (SPCM-AQRH-14-TR, Excelitas), and a time-correlated single-photon counting unit (TCSPC TimeHarp 260 PICO Dual, PicoQuant, temporal resolution of 250 ps) was used to collect fluorescence data. The microscope was calibrated with a Rhodamine 110 solution excited at $\lambda = 560$ nm, yielding a radius of $\omega_r = 504 \pm 40$ nm for the detection volume in the lateral dimension. The afterpulsing effects of the avalanche photodiode were removed by applying fluorescence lifetime correlation spectroscopy (FLCS) [88, 89]. The fluorescence data was corrected and autocorrelated using the commercial software SymPhoTime 64 (Picoquant).

TEM was carried out with a JEOL JEM-2200FS field emission TEM. The energy filtering transmission electron microscope (EFTEM) was operated at an acceleration voltage of 200 kV. Zero-loss filtered micrographs ($\Delta E \approx 0$ eV) were taken with a bottom mounted CMOS camera system (OneView, Gatan) and the images were processed with a digital image processing software (Digital Micrograph 3.11, Gatan). The diluted micelle dispersions ($c = 0.1$ g L^{-1}, $V = 10$ μL) were dropped on a carbon-coated copper grid, and the residual solvent was removed directly by blotting

with a filter paper, followed by drying of the coated copper grid in vacuo (24 h, $1 \cdot 10^{-5}$ mbar). The samples were stained for 5 min with RuO_4 vapor, which was formed in situ from $RuCl_3$ hydrate and an aqueous NaOCl solution. Afterwards, the samples were kept in a fume hood for at least 1 h to ensure the complete removal of any unreacted RuO_4. The sizes of the P*L*LA patches were determined with the software Fiji using the freehand selection tool and measuring 150 patches from multiple positions [90].

4.3 | Polymer Syntheses

4.3.1 | Hydroxy Terminated Polystyrene-block-Polybutadiene Macroinitiator (SB-OH)

The SB-OH macroinitiator was prepared by sequential living anionic polymerization of styrene and 1,3-butadiene in toluene followed by end-capping with ethylene oxide as published elsewhere [80]. Briefly, styrene was polymerized at 25°C for 4 h using *sec*-BuLi as the initiator. Subsequently, butadiene was added and allowed to polymerize at 40°C for 5 h. After complete conversion, the reaction mixture was cooled to 5°C and a 5-fold molar excess of ethylene oxide was added followed by stirring for 30 min at 25°C. The polymer was terminated with a mixture of acetic acid/methanol (1/5 (v/v)) and isolated by precipitation from methanol. The product was filtered and dried in vacuo (2×10^{-2} mbar) at 40°C.

4.3.2 | PS-*b*-PB-*b*-P*L*LA (SBL)

PS-*b*-PB-*b*-P*L*LA triblock terpolymers were prepared according to the literature [91]. To SB-OH in DCM ($c \approx 150\,g\,L^{-1}$) the respective amount of *L*-lactide was added and stirred at 25°C for 10 min under argon. DBU (10 eq with respect to OH end groups) was added, and the reaction mixture was stirred for 10 min at 25°C. Subsequently, benzoic acid (equimolar amount to DBU) was added to stop the reaction, and the mixture was stirred for 30 min. The product was precipitated from MeOH, filtered, and dried in vacuo (1×10^{-5} mbar).

4.3.3 | Hydrogenation

The PS-*b*-PE-*b*-P*L*LA triblock terpolymers were obtained by hydrogenation of the corresponding SBL precursors via homogeneous catalysis in toluene at 60°C and 60 bar H_2 pressure for 3 days using Wilkinson's catalyst ($RhCl(PPH_3)_3$, 1 mol% with respect to the number of double bonds in the PB block). For purification, the polymer was refluxed with small amounts of concentrated hydrochloric acid and precipitated from methanol. Additionally, SEL-1 was dissolved in toluene at 70°C and precipitated from acetone/isopropanol (1/1 (v/v)), centrifuged, and dried in vacuo (1×10^{-5} mbar).

4.3.4 | Hydroxy Terminated and Fluorescently Labeled P*D*LA Homopolymer (P*D*LA$_{62}$ and P*D*LA$_{62}$-RB)

P*D*LA$_{62}$ and P*D*LA$_{62}$-RB were prepared as published in previous work [79]. Briefly, P*D*LA$_{62}$ was synthesized by organo-catalyzed ring-opening polymerization of *L*-lactide employing HEB*i*B as the initiator and DBU as the catalyst. P*D*LA$_{62}$-RB was obtained by esterification of the hydroxy end group with sulforhodamine B acid chloride.

4.4 | Preparation of wCCMs and SC Loading

Preparation of wCCMs via CDSA was carried out with a Crystal 16 instrument (Technobis Crystallization Systems). The SEL triblock terpolymers were dispersed at a concentration of $c = 10\,g\,L^{-1}$ in the respective solvent (THF) or solvent mixture (Xyl/CH = 80/20 (v/v)) using 1.5 mL vials equipped with a small stirring bar, and the following heating and cooling protocol was conducted. First, the samples were dissolved at 60°C for 1 h, followed by erasing any thermal history at 65°C (THF) or 80°C (Xyl/CH = 80/20 (v/v)) for 10 min. While slowly stirring (50 rpm) the solutions were cooled to the crystallization temperature of the PE block (T_c(PE), Table S1) at a cooling rate of $0.5\,K\,min^{-1}$ and held at this temperature for 24 h. Subsequently, the dispersions were cooled to −10°C at $0.1\,K\,min^{-1}$, held for 1 h, and finally heated to 20°C at $0.5\,K\,min^{-1}$.

For SCDSA experiments, P*D*LA$_{62}$ dissolved in THF ($c = 10\,g\,L^{-1}$, $V = 36\,\mu L$ [for SEL-1] or $54\,\mu L$ [for SEL-2]) was added to the SEL wCCM dispersion ($c = 10\,g\,L^{-1}$ in Xyl/CH = 80/20 [v/v], $V = 200\,\mu L$), employing a 2:1 weight ratio with respect to the enantiomeric P*L*LA and P*D*LA blocks (amount of THF after the addition ≈ 15 vol-% for SEL-1 and ≈ 21 vol-% for SEL-2). Afterwards, the dispersion was aged at 25°C for 1 week, and the remaining THF was allowed to evaporate. Fluorescently labeled wCCMs were prepared analogously using P*D*LA$_{62}$-RB.

Acknowledgments

Financial support by the German Research Foundation (project SCHM2428/3-1) is gratefully acknowledged. We thank Prof. Andreas Greiner for helpful discussions, Rika Schneider for SEC measurements, Christian Hils for help in polymer synthesis, and Dr. Ulrich Mansfeld for assistance with TEM measurements. R.S. acknowledges support by the Graduate School of University of Bayreuth. We acknowledge support from the keylabs "*Electron and Optical Microscopy*", "*Synthesis and Molecular Characterization*", and "*Optical Spectroscopy*" of the Bavarian Polymer Institute (BPI) at the University of Bayreuth, and Corbion for the donation of *D*- and *L*-lactide.

References

1. J. Du and R. K. O'Reilly, "Anisotropic Particles With Patchy, Multicompartment and Janus Architectures: Preparation and Application," *Chemical Society Reviews* 40 (2011): 2402–2416.

2. K. Zhang, M. Jiang, and D. Chen, "Self-Assembly of Particles—The Regulatory Role of Particle Flexibility," *Progress in Polymer Science* 37 (2012): 445–486.

3. M. Karayianni and S. Pispas, "Block Copolymer Solution Self-Assembly: Recent Advances, Emerging Trends, and Applications," *Journal of Polymer Science* 59 (2021): 1874–1898.

4. I. W. Wyman and G. Liu, "Micellar Structures of Linear Triblock Terpolymers: Three Blocks but Many Possibilities," *Polymer* 54 (2013): 1950–1978.

5. A. H. Gröschel and A. H. E. Müller, "Self-Assembly Concepts for Multicompartment Nanostructures," *Nanoscale* 7 (2015): 11841–11876.

6. U. Tritschler, S. Pearce, J. Gwyther, G. R. Whittell, and I. Manners, "50th Anniversary Perspective: Functional Nanoparticles From the Solution Self-Assembly of Block Copolymers," *Macromolecules* 50 (2017): 3439–3463.

7. W. Li, H. Palis, R. Mérindol, J. Majimel, S. Ravaine, and E. Duguet, "Colloidal Molecules and Patchy Particles: Complementary Concepts, Synthesis and Self-Assembly," *Chemical Society Reviews* 49 (2020): 1955–1976.

8. A. K. Pearce, T. R. Wilks, M. C. Arno, and R. K. O'Reilly, "Synthesis and Applications of Anisotropic Nanoparticles With Precisely Defined Dimensions," *Nature Reviews Chemistry* 5 (2021): 21–45.

9. T. Pelras, C. S. Mahon, and M. Müllner, "Synthesis and Applications of Compartmentalised Molecular Polymer Brushes," *Angewandte Chemie, International Edition* 57 (2018): 6982–6994.

10. A. O. Moughton, M. A. Hillmyer, and T. P. Lodge, "Multicompartment Block Polymer Micelles," *Macromolecules* 45 (2012): 2–19.

11. I. Mirza and S. Saha, "Biocompatible Anisotropic Polymeric Particles: Synthesis, Characterization, and Biomedical Applications," *ACS Applied Bio Materials* 3 (2020): 8241–8270.

12. Q. Yang and K. Loos, "Janus Nanoparticles Inside Polymeric Materials: Interfacial Arrangement Toward Functional Hybrid Materials," *Polymer Chemistry* 8 (2017): 641–654.

13. A. Walther and A. H. E. Müller, "Janus Particles: Synthesis, Self-Assembly, Physical Properties, and Applications," *Chemical Reviews* 113 (2013): 5194–5261.

14. Y. Shao, Y. Ye, D. Sun, and Z. Yang, "Polymer-Derived Janus Particles at Multiple Length Scales," *Macromolecules* 55 (2022): 6297–6310.

15. C. Marschelke, A. Fery, and A. Synytska, "Janus Particles: From Concepts to Environmentally Friendly Materials and Sustainable Applications," *Colloid & Polymer Science* 298 (2020): 841–865.

16. X. Fan, J. Yang, X. J. Loh, and Z. Li, "Polymeric Janus Nanoparticles: Recent Advances in Synthetic Strategies, Materials Properties, and Applications," *Macromolecular Rapid Communications* 40 (2019): 1800203.

17. R. Deng, F. Liang, J. Zhu, and Z. Yang, "Recent Advances in the Synthesis of Janus Nanomaterials of Block Copolymers," *Materials Chemistry Frontiers* 1 (2017): 431–443.

18. G. Agrawal and R. Agrawal, "Janus Nanoparticles: Recent Advances in Their Interfacial and Biomedical Applications," *ACS Applied Nano Materials* 2 (2019): 1738–1757.

19. C. Hils, I. Manners, J. Schöbel, and H. Schmalz, "Patchy Micelles With a Crystalline Core: Self-Assembly Concepts, Properties, and Applications," *Polymers* 13 (2021): 1481.

20. I. S. Jo, S. Lee, J. Zhu, T. S. Shim, and G. R. Yi, "Soft Patchy Micelles," *Current Opinion in Colloid & Interface Science* 30 (2017): 97–105.

21. S. Karadkar, A. Tiwari, and A. C. Chaskar, "Recent Advancements in Janus Nanoparticle-Based Biosensing Platforms," *International Nano Letters* 13 (2023): 93–115.

22. Y. Yi, L. Sanchez, Y. Gao, and Y. Yu, "Janus Particles for Biological Imaging and Sensing," *Analyst* 141 (2016): 3526–3539.

23. L. C. Bradley, W. H. Chen, K. J. Stebe, and D. Lee, "Janus and Patchy Colloids at Fluid Interfaces," *Current Opinion in Colloid & Interface Science* 30 (2017): 25–33.

24. A. Walther, M. Hoffmann, and A. H. E. Müller, "Emulsion Polymerization Using Janus Particles as Stabilizers," *Angewandte Chemie, International Edition* 47 (2008): 711–714.

25. Y. Lan, J. Choi, H. Li, et al., "Janus Particles with Varying Configurations for Emulsion Stabilization," *Industrial and Engineering Chemistry Research* 58 (2019): 20961–20968.

26. R. Bahrami, T. I. Löbling, A. H. Gröschel, H. Schmalz, A. H. E. Müller, and V. Altstädt, "The Impact of Janus Nanoparticles on the Compatibilization of Immiscible Polymer Blends Under Technologically Relevant Conditions," *ACS Nano* 8, no. 10 (2014): 10048–10056.

27. R. Bahrami, T. I. Löbling, H. Schmalz, A. H. E. Müller, and V. Altstädt, "Synergistic Effects of Janus Particles and Triblock Terpolymers on Toughness of Immiscible Polymer Blends," *Polymer* 109 (2017): 229–237.

28. A. Walther, K. Matussek, and A. H. E. Müller, "Engineering Nanostructured Polymer Blends With Controlled Nanoparticle Location Using Janus Particles," *ACS Nano* 2 (2008): 1167–1178.

29. H. L. He and F. X. Liang, "Interfacial Engineering of Polymer Blend with Janus Particle as Compatibilizer," *Chinese Journal of Polymer Science* 41 (2023): 500–515.

30. C. Chen, L. Zhang, N. Wang, D. Sun, and Z. Yang, "Janus Composite Particles and Interfacial Catalysis Thereby," *Macromolecular Rapid Communications* 44 (2023): 2300280.

31. J. Wu, C. Feng, X. Ma, et al., "Efficient Fabrication of Janus Particles with Active Groups and Application in Emulsion Stabilization and Interfacial Catalysis," *ACS Applied Polymer Materials* 6 (2024): 1740–1750.

32. D. J. Lunn, J. R. Finnegan, and I. Manners, "Self-Assembly of "Patchy" Nanoparticles: A Versatile Approach to Functional Hierarchical Materials," *Chemical Science* 6 (2015): 3663–3673.

33. Z. Zhang and S. C. Glotzer, "Self-Assembly of Patchy Particles," *Nano Letters* 4 (2004): 1407–1413.

34. B. Jin, Y. Chen, Y. Luo, and X. Li, "Precise and Controllable Assembly of Block Copolymers," *Chinese Journal of Chemistry* 41 (2023): 93–110.

35. Y. Lu, J. Lin, L. Wang, L. Zhang, and C. Cai, "Self-Assembly of Copolymer Micelles: Higher-Level Assembly for Constructing Hierarchical Structure," *Chemical Reviews* 120 (2020): 4111–4140.

36. A. Piloni, A. Walther, and M. H. Stenzel, "Compartmentalized Nanoparticles in Aqueous Solution Through Hierarchical Self-Assembly of Triblock Glycopolymers," *Polymer Chemistry* 9 (2018): 4132–4142.

37. T. I. Löbling, O. Borisov, J. S. Haataja, O. Ikkala, A. H. Gröschel, and A. H. E. Müller, "Rational Design of ABC Triblock Terpolymer Solution Nanostructures with Controlled Patch Morphology," *Nature Communications* 7 (2016): 1–10.

38. A. H. Gröschel, A. Walther, T. I. Löbling, F. H. Schacher, H. Schmalz, and A. H. E. Müller, "Guided Hierarchical Co-Assembly of Soft Patchy Nanoparticles," *Nature* 503, no. 7475 (2013): 247–251.

39. C. Hils, M. Dulle, G. Sitaru, et al., "Influence of Patch Size and Chemistry on the Catalytic Activity of Patchy Hybrid Nonwovens," *Nanoscale Advances* 2 (2020): 438–452.

40. J. Schöbel, M. Karg, D. Rosenbach, G. Krauss, A. Greiner, and H. Schmalz, "Patchy Wormlike Micelles With Tailored Functionality by Crystallization-Driven Self-Assembly: A Versatile Platform for Mesostructured Hybrid Materials," *Macromolecules* 49 (2016): 2761–2771.

41. J. Schöbel, C. Hils, A. Weckwerth, et al., "Strategies for the Selective Loading of Patchy Worm-Like Micelles With Functional Nanoparticles," *Nanoscale* 10 (2018): 18257–18268.

42. J. Schöbel, M. Burgard, C. Hils, et al., "Bottom-Up Meets Top-Down: Patchy Hybrid Nonwovens as an Efficient Catalysis Platform," *Angewandte Chemie, International Edition* 56 (2017): 405–408.

43. A. Frank, C. Hils, M. Weber, K. Kreger, H. Schmalz, and H.-W. Schmidt, "Hierarchical Superstructures by Combining Crystallization-Driven and Molecular Self-Assembly," *Angewandte Chemie, International Edition* 60 (2021): 21767–21771.

44. A. Frank, M. Weber, C. Hils, et al., "Functional Mesostructured Electrospun Polymer Nonwovens with Supramolecular Nanofibers," *Macromolecular Rapid Communications* 43 (2022): 2200052.

45. S. Ganda and M. H. Stenzel, "Concepts, Fabrication Methods and Applications of Living Crystallization-Driven Self-Assembly of Block Copolymers," *Progress in Polymer Science* 101 (2020): 101195.

46. L. MacFarlane, C. Zhao, J. Cai, H. Qiu, and I. Manners, "Emerging Applications for Living Crystallization-Driven Self-Assembly," *Chemical Science* 12 (2021): 4661–4682.

47. J. Ma, G. Lu, X. Huang, and C. Feng, "π-Conjugated-Polymer-Based Nanofibers Through Living Crystallization-Driven Self-Assembly: Preparation, Properties and Applications," *Chemical Communications* 57 (2021): 13259–13274.

48. S. Mahapatra, P. Dey, and G. Ghosh, "Controlled Synthesis of Cylindrical Micelles via Crystallization-Driven Self-Assembly (CDSA) and Applications," *Polymer Journal* 56 (2024): 949–975.

49. J. Schmelz, A. E. Schedl, C. Steinlein, I. Manners, and H. Schmalz, "Length Control and Block-Type Architectures in Worm-Like Micelles With Polyethylene Cores," *Journal of the American Chemical Society* 134 (2012): 14217–14225.

50. A. M. Oliver, J. Gwyther, M. A. Winnik, and I. Manners, "Cylindrical Micelles With "Patchy" Coronas From the Crystallization-Driven Self-Assembly of ABC Triblock Terpolymers With a Crystallizable Central Polyferrocenyldimethylsilane Segment," *Macromolecules* 51 (2018): 222–231.

51. A. M. Oliver, R. J. Spontak, and I. Manners, "Solution Self-Assembly of ABC Triblock Terpolymers with a Central Crystallizable Poly(ferrocenyldimethylsilane) Core-Forming Segment," *Polymer Chemistry* 10 (2019): 2559–2569.

52. J. Schmelz, M. Karg, T. Hellweg, and H. Schmalz, "General Pathway Toward Crystalline-Core Micelles With Tunable Morphology and Corona Segregation," *ACS Nano* 5 (2011): 9523–9534.

53. T. Rudolph, A. Nunns, S. Stumpf, C. Pietsch, and F. H. Schacher, "Hierarchical Self-Assembly of Double-Crystalline Poly(ferrocenyldimethylsilane)-*block*-poly(2-*iso*-propyl-2-oxazoline) (PFDMS-*b*-PiPrOx) Block Copolymers," *Macromolecular Rapid Communications* 36 (2015): 1651–1657.

54. C. Hils, J. Schmelz, M. Drechsler, and H. Schmalz, "Janus Micelles by Crystallization-Driven Self-Assembly of an Amphiphilic, Double-Crystalline Triblock Terpolymer," *Journal of the American Chemical Society* 143 (2021): 15582–15586.

55. M. Vespa, L. R. MacFarlane, Z. M. Hudson, and I. Manners, "Crystallization-Driven Self-Assembly of Poly(3-Hexylthiophene)-*b*-Poly(2,5-Bis(2-Ethylhexyloxy)p-Phenylene), a π-Conjugated Diblock Copolymer With a Rigid Rod Corona-Forming Block," *Polymer Chemistry* 15 (2024): 1839–1850.

56. J. Kim, W. Chung, D. Kim, et al., "Semi-Conductive Micellar Networks of All-Conjugated Diblock and Triblock Copolymer Blends," *Chemical Communications* 59 (2023): 3578–3581.

57. Y. Yin, S. Chen, S. Zhu, et al., "Tailoring Cocrystallization and Microphase Separation in Rod–Rod Block Copolymers for Field-Effect Transistors," *Macromolecules* 54 (2021): 4571–4581.

58. H. Shaikh, X. H. Jin, R. L. Harniman, R. M. Richardson, G. R. Whittell, and I. Manners, "Solid-State Donor–Acceptor Coaxial Heterojunction Nanowires via Living Crystallization-Driven Self-Assembly," *Journal of the American Chemical Society* 142 (2020): 13469–13480.

59. Z. Gao, X. Zhang, B. Zheng, J. Gu, and Z. Tong, "Creation of Segmented Platelets With Diverse Crystalline Cores Using Double Crystalline Triblock Copolymers," *Journal of the American Chemical Society* 147 (2025): 5172–5181.

60. R. M. Michell, V. Ladelta, E. Da Silva, A. J. Müller, and N. Hadjichristidis, "Poly(Lactic Acid) Stereocomplexes Based Molecular Architectures: Synthesis and Crystallization," *Progress in Polymer Science* 146 (2023): 101742.

61. Z. Li, B. H. Tan, T. Lin, and C. He, "Recent Advances in Stereocomplexation of Enantiomeric PLA-Based Copolymers and Applications," *Progress in Polymer Science* 62 (2016): 22–72.

62. R. Liu, B. He, D. Li, Y. Lai, J. Z. Tang, and Z. Gu, "Stabilization of pH-Sensitive mPEG–PH–PLA Nanoparticles by Stereocomplexation Between Enantiomeric Polylactides," *Macromolecular Rapid Communications* 33 (2012): 1061–1066.

63. W. Zhang, D. Zhang, X. Fan, G. Bai, G. Yuming, and Z. Hu, "Stable Stereocomplex Micelles From Y-Shaped Amphiphilic Copolymers MPEG–(scPLA)2: Preparation and Characteristics," *RSC Advances* 6 (2016): 20761–20771.

64. S. Noack, D. Schanzenbach, J. Koetz, and H. Schlaad, "Polylactide-Based Amphiphilic Block Copolymers: Crystallization-Induced Self-Assembly and Stereocomplexation," *Macromolecular Rapid Communications* 40 (2019): 1800639.

65. A. M. Desyatskova, E. V. Kuznetsova, Y. A. Puchkova, et al., "Effect of Stereocomplex Formation between Enantiomeric Poly(l,l-lactide) and Poly(d,d-lactide) Blocks on Self-Organization of Amphiphilic Poly(lactide)-block-Poly(ethylene oxide) Copolymers in Dilute Aqueous Solution," *Mendeleev Communications* 33 (2023): 86–89.

66. X. Chang, H. Mao, G. Shan, Y. Bao, and P. Pan, "Tuning the Thermoresponsivity of Amphiphilic Copolymers via Stereocomplex Crystallization of Hydrophobic Blocks," *ACS Macro Letters* 8 (2019): 357–362.

67. H. Niu, J. Li, Q. Cai, et al., "Molecular Stereocomplexation for Enhancing the Stability of Nanoparticles Encapsulated in Polymeric Micelles for Magnetic Resonance Imaging," *Langmuir* 36 (2020): 13881–13889.

68. X. Fan, Z. Wang, D. Yuan, Y. Sun, Z. Li, and C. He, "Novel Linear-Dendritic-Like Amphiphilic Copolymers: Synthesis and Self-Assembly Characteristics," *Polymer Chemistry* 5, no. 13 (2014): 4069–4075.

69. L. Sun, A. Pitto-Barry, N. Kirby, et al., "Structural Reorganization of Cylindrical Nanoparticles Triggered by Polylactide Stereocomplexation," *Nature Communications* 5 (2014): 1–9.

70. Z. Li, D. Yuan, X. Fan, B. H. Tan, and C. He, "Poly(Ethylene Glycol) Conjugated Poly(Lactide)-Based Polyelectrolytes: Synthesis and Formation of Stable Self-Assemblies Induced by Stereocomplexation," *Langmuir* 31 (2015): 2321–2333.

71. X. Yu, X. Guo, Y. Fang, Z. Fan, M. Guo, and B. Cheng, "Topological Structure-induced Self-Assembly of Highly Asymmetric PLLA-*b*-QPDMAEMA Block Copolymers in Solution: Linear versus Bottlebrush," *European Polymer Journal* 202 (2024): 112648.

72. X. Zhang, B. H. Tan, and C. He, "Tailoring the LCST of PNIPAAM-*b*-PLA-*b*-PNIPAAM Triblock Copolymers via Stereocomplexation," *Macromolecular Rapid Communications* 34 (2013): 1761–1766.

73. F. K. Wolf, A. M. Hofmann, and H. Frey, "Poly(Isoglycerol Methacrylate)-*b*-Poly(*D* or *L*-Lactide) Copolymers: A Novel Hydrophilic Methacrylate as Building Block for Supramolecular Aggregates," *Macromolecules* 43 (2010): 3314–3324.

74. Y. Xie, W. Yu, T. Xia, R. K. O'Reilly, and A. P. Dove, "Stereocomplex-Driven Morphological Transition of Coil–Rod–Coil Poly(Lactic Acid)-Based Cylindrical Nanoparticles," *Macromolecules* 56, no. 19 (2023): 7689–7697.

75. D. Portinha, L. Bouteiller, S. Pensec, A. Richez, and C. Chassenieux, "Influence of Preparation Conditions on the Self-Assembly by Stereocomplexation of Polylactide Containing Diblock Copolymers," *Macromolecules* 37 (2004): 3401–3406.

76. D. Portinha, F. Boué, L. Bouteiller, et al., "Stable Dispersions of Highly Anisotropic Nanoparticles Formed by Cocrystallization of Enantiomeric Diblock Copolymers," *Macromolecules* 40 (2007): 4037–4042.

77. X. Hou, Q. Li, and A. Cao, "In Situ Aggregates of Enantiomeric Poly(Styrene)-*block*-Poly(Lactide) Diblock Copolymers via

Stereocomplexation in a Non-selective Solvent," *Macromolecular Chemistry and Physics* 214 (2013): 1569–1579.

78. R. Schaller, C. Hils, M. Karg, and H. Schmalz, "Surface-Compartmentalized Micelles by Stereocomplex-Driven Self-Assembly," *Macromolecular Rapid Communications* 44 (2023): 2200682.

79. R. Schaller, M. Schmidt, K. Schweimer, and H. Schmalz, "Patchy Stereocomplex Micelles as Efficient Compatibilizers for Polymer Blends," *Polymer Chemistry* 15 (2024): 3100–3112.

80. N. Janoszka, S. Azhdari, C. Hils, D. Coban, H. Schmalz, and A. H. Gröschel, "Morphology and Degradation of Multicompartment Microparticles Based on Semi-Crystalline Polystyrene-block-Polybutadiene-block-Poly(*L*-Lactide) Triblock Terpolymers," *Polymers* 13 (2021): 4358.

81. H. Schmalz, J. Schmelz, M. Drechsler, et al., "Thermo-Reversible Formation of Wormlike Micelles With a Microphase-Separated Corona From a Semicrystalline Triblock Terpolymer," *Macromolecules* 41 (2008): 3235–3242.

82. A. S. Zalusky, R. Olayo-Valles, J. H. Wolf, and M. A. Hillmyer, "Ordered Nanoporous Polymers From Polystyrene-Polylactide Block Copolymers," *Journal of the American Chemical Society* 124 (2002): 12761–12773.

83. J. Schmelz and H. Schmalz, "Corona Structure on Demand: Tailor-Made Surface Compartmentalization in Worm-Like Micelles via Random Cocrystallization," *Polymer* 53 (2012): 4333–4337.

84. P. van de Witte, A. Boorsma, H. Esselbrugge, P. J. Dijkstra, J. W. A. van den Berg, and J. Feijen, "Differential Scanning Calorimetry Study of Phase Transitions in Poly(Lactide)−Chloroform−Methanol Systems," *Macromolecules* 29 (1996): 212–219.

85. V. Ladelta, K. Ntetsikas, G. Zapsas, and N. Hadjichristidis, "Non-Covalent PS–SC–PI Triblock Terpolymers via Polylactide Stereocomplexation: Synthesis and Thermal Properties," *Macromolecules* 55 (2022): 2832–2843.

86. H. Tsuji, "Poly(Lactic Acid) Stereocomplexes: A Decade of Progress," *Advanced Drug Delivery Reviews* 107 (2016): 97–135.

87. H. Zettl, W. Häfner, A. Böker, et al., "Fluorescence Correlation Spectroscopy of Single Dye-Labeled Polymers in Organic Solvents," *Macromolecules* 37 (2004): 1917–1920.

88. P. Kapusta, M. Wahl, A. Benda, M. Hof, and J. Enderlein, "Fluorescence Lifetime Correlation Spectroscopy," *Journal of Fluorescence* 17 (2007): 43–48.

89. J. Enderlein, I. Gregor, D. Patra, T. Dertinger, and U. B. Kaupp, "Performance of Fluorescence Correlation Spectroscopy for Measuring Diffusion and Concentration," *ChemPhysChem* 6 (2005): 2324–2336.

90. J. Schindelin, I. Arganda-Carreras, E. Frise, et al., "Fiji: An Open-Source Platform for Biological-Image Analysis," *Nature Methods* 9 (2012): 676–682.

91. W. Yu, M. Inam, J. R. Jones, A. P. Dove, and R. K. O'Reilly, "Understanding the CDSA of Poly(Lactide) Containing Triblock Copolymers," *Polymer Chemistry* 8 (2017): 5504–5512.

Supporting Information

Additional supporting information can be found online in the Supporting Information section.